

Investigation of Analytical Models for Surface-Mounted Permanent Magnet Motor Using Voltage Source Inverter

Zhaokai Li¹, Member, IEEE, Xiaoyan Huang¹, Member, IEEE, Zixuan Liu, Lijian Wu¹, Senior Member, IEEE, Teng Long¹, Yuzheng Chen, Xinru Li¹, Wucheng Ying¹, Boyang Shen¹, and Yutong Fang¹, Senior Member, IEEE

Abstract—This article analyzed and compared the complex permeance model (CPM) and nonlinear analytical model (NAM) for surface-mounted permanent magnet (SPM) motor using a voltage source inverter (VSI). For linear CPM, the slotting effect is represented using the improved complex permeance function that describes the real slot shape rather than infinitely deep slot. NAM is extended from CPM and it replaces the magnetic potential drop of stator iron by the equivalent virtual current in the slot-opening and tooth-tip to account for the nonlinearity effect. The nonlinear inductance of SPM motor including the main phase inductance, slot leakage inductance, tooth-tip leakage inductance, and end winding leakage inductance is calculated using the frozen permeability method, which is the key to solve the electric circuit with VSI. The instantaneous back electromotive force (EMF) is calculated from the nonlinear back EMF coefficient and the back EMF neglecting iron nonlinearity. The electromagnetic torque obtained from motor model is used in the mechanical model and then the rotational speed and rotor position are obtained for the electric circuit model. Hence, the iterative solving process for the motor system is established to calculate the transient performance of SPM motor using VSI. Compared with CPM, NAM can greatly improve the calculation accuracy, which is also validated by both finite-element model and experiment. Besides, the proposed NAM is computationally efficient, which is useful for both motor design and motor control.

Index Terms—Analytical model, complex permeance model (CPM), iron nonlinearity, voltage source inverter (VSI).

Manuscript received October 9, 2021; revised February 20, 2022; accepted May 18, 2022. Date of publication May 23, 2022; date of current version July 19, 2022. Paper 2021-IPCC-1228.R1, presented at the 2019 IEEE Energy Conversion Congress and Exposition, Baltimore, MD, USA, Sep. 29-Oct. 3, and approved for publication in the IEEE TRANSACTIONS ON INDUSTRY APPLICATIONS by the Industrial Power Converter Committee of the IEEE Industry Applications Society. This work was supported in part by the National Key R&D Program of China under Grant 2019YFE0123500, in part by the Zhejiang Provincial Ten-Thousand-Talent Plan under Grant 2019R52003, and in part by the Fundamental Research Funds for the Central Universities under Grant 2021FZZX001-13. (Corresponding author: Xiaoyan Huang.)

Zhaokai Li, Xiaoyan Huang, Zixuan Liu, Lijian Wu, and Yutong Fang are with the Zhejiang University, Hangzhou 310027, China (e-mail: lzk_zju@zju.edu.cn; xiaoyanhuan@zju.edu.cn; eelzx@zju.edu.cn; ljw@zju.edu.cn; yutong@zju.edu.cn).

Teng Long, Xinru Li, Wucheng Ying, and Boyang Shen are with the Department of Engineering, University of Cambridge, CB2 1PZ Cambridge, U.K. (e-mail: tl322@cam.ac.uk; xl418@cam.ac.uk; wy256@cam.ac.uk; bs506@cam.ac.uk).

Yuzheng Chen is with the Department of Electrical and Electronic Engineering, University of Nottingham, NG7 2RD Nottingham, U.K. (e-mail: yuzheng.chen@nottingham.ac.uk).

Color versions of one or more figures in this article are available at <https://doi.org/10.1109/TIA.2022.3176846>.

Digital Object Identifier 10.1109/TIA.2022.3176846

I. INTRODUCTION

PERMANENT magnet (PM) motors have drawn great attention due to the high efficiency and simple structure. For the permanent magnet synchronous motor (PMSM), both design method and control strategy play an important part in improving the electromagnetic performance to the greatest extend. However, most researches focus on the motor design or motor control separately to reduce the computational time and therefore the motor systems will lose some advantage in the real applications. Thus, cosimulation receives massive attention for the whole system design [1]–[16].

For analyzing the PM motor with an external circuit, the nonlinear winding inductance and back electromotive force (EMF) should be extracted from the motor model first. There are three methods to build the motor model: numerical method, circuit-based method, and analytical method. For the numerical method, finite-element model (FEM) can accurately consider the nonlinearity and complex geometry of the PM motors and it is capable to predict the electromagnetic performance of most PM motors accurately. The cosimulation combining FEM software with circuit simulation software was proposed for linear induction motor [2], synchronous reluctance motor [3], brushless direct-current (BLDC) motor [4], [5], doubly salient PM motor [6], PM synchronous motor [7], [8], etc. Although the FEM coupled with external circuit can be instantaneously solved in the cosimulation, its high prediction accuracy will accompany with large computational burden, making it unpractical for motor optimization. To overcome this disadvantage, offline calculation of FEM is often performed to establish the nonlinear motor model in the electric circuit simulation. The electromagnetic features of the motor are extracted from FEM results and they are represented using the looking up table [9]–[11] or nonlinear function [12]–[16]. Hence, only little computational resource is required for analyzing the transient characteristic of the motor coupled with electric circuit. However, the motor models from offline FEM calculation are still different from the real-time characteristic of real motors.

For the circuit-based method, magnetic circuit model (MCM) is proposed to analyze the nonlinearity of electric motors but its accuracy and computational speed are significantly influenced by the size of magnetic circuit matrix [17], [18]. Fleming and

Edrington [19] provided a novel MCM for switched reluctance motor in the real-time emulation. Fukuoka *et al.* [20] introduced a reluctance network for planetary-type magnetic gear and then performed transient analyses at different loads. Cao *et al.* [21] optimized the surface-mounted permanent magnet (SPM) motor with equivalent magnetic network with high accuracy. Mine *et al.* [22] presented two simple techniques to speed up the solving process for magnetic reluctance in the induction machines and obtained their transient behavior with high accuracy. Hence, the MCM (including reluctance network) can be a good substitute for FEM in the transient analysis of PM motors. Nevertheless, MCM shows poor performance to predict magnetic field with complex flux path, which leads to either low accuracy or huge computation.

The linear analytical model can only present the linear electromagnetic performance of PM motors [23], [24]. It can be used to analyze the torque ripple of BLDC motors coupled with external circuit [25]. Xuan *et al.* [26] proposed the winding function to obtain the inductance of fractional slot PM motors and then analyzed the three-phase short circuit current. However, these analytical models are not suitable for cosimulation since they cannot improve the calculation accuracy due to their linear property. To solve this problem, the nonlinear analytical models (NAMs) were proposed in [27]–[31] and the equivalent current was introduced to represent iron nonlinearity. However, these models have been verified using current source at steady-state condition and there is a lack of research about the NAMs with voltage source inverter (VSI).

This article investigates a NAM for predicting the transient performance of SPM motor using VSI. The back EMF, inductance, and torque considering both slotting effect and nonlinearity effect are extracted from the NAM using the nonlinearity factor. Coupled with electric circuit model and mechanical model, the transient performance of SPM motor using VSI considering pulsewidth modulation (PWM) effect can be obtained with great calculation accuracy and high calculation efficiency. The differences between complex permeance model (CPM) and NAM are compared and investigated to show the improvement for motor control simulation, where the constant and linear parameters are usually preferred to represent the nonlinear motor and therefore introduce large errors. Finally, FEM cosimulation and experiment are carried out to verify the proposed model.

The rest of the article is organized as follows. Section I summarizes the recent research about the motor model that requires high calculation accuracy and high calculation efficiency. Under the circumstance, the NAM can be the perfect candidate for analyzing the transient performance of SPM motor using VSI. In Section II, the NAM that combined MCM and CPM is proposed to predict the magnetic field distribution of SPM motor. Then, the electric circuit model transforms the magnetic field from NAM into the circuit component to obtain the next phase current. The mechanical model is used to calculate the next rotor position based on the predicted torque using NAM. Their coupling is essential to obtain the transient performance of SPM motor. Section III analyzed the transient performance of a 15-slot/4-pole prototype motor at constant speed and at constant torque using CPM, NAM, FEM, and experiment. They all verify

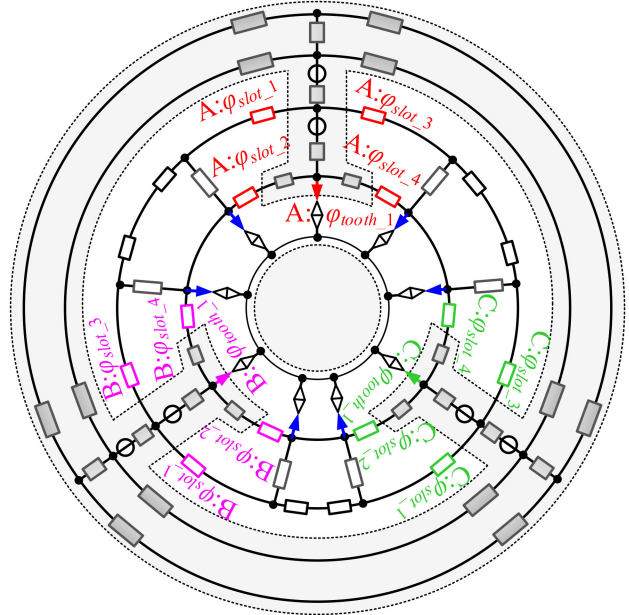


Fig. 1. Overall magnetic model for a three-slot SPM motor using NAM.

the high calculation accuracy and efficiency of NAM. Finally, Section IV concludes this article.

II. ANALYTICAL MODEL WITH VSI

The analytical model with voltage inverter consists of three parts: magnetic model, electric circuit model, and mechanical model. In the motor model, iron nonlinearity is represented by the equivalent current in the slot-opening and tooth-tip. Hence, the analytical air-gap field of SPM motor can be directly obtained. In the electric circuit model, the VSI with semiconductor devices is modeled according to the circuit theory, whereas the nonlinear winding inductance and back EMF are derived from the air-gap field of SPM motors. In the mechanical model, the motion state is obtained using the predicted torque from the NAM. By manipulating these mathematical models, the performance of SPM motor will be iteratively obtained considering the nonlinearity effect and the influence of VSI.

A. Magnetic Model of SPM Motor

To model the iron nonlinearity and slotting effect, the NAM combining MCM with CPM is proposed to calculate the magnetic field of the whole motor. Fig. 1 gives the overall model to represent the SPM motor. The stator iron and slot region are replaced by the magnetic reluctance, whereas the air-gap field is represented using the air-gap flux source. The rotor position only affects the value of air-gap flux source, whereas the connection of magnetic reluctance in the MCM stays unchanged. The rotor permeability is assumed infinite because the rotor iron of SPM motor is usually thick enough to make the rotor flux density away from the saturation level for better performance [27]–[30].

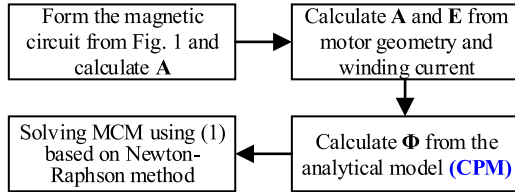


Fig. 2. Flowchart of calculating MCM.

Based on Kirchhoff's laws, the mathematic solution of the MCM for SPM motor is represented as [28]

$$f(\mathbf{V}) = \mathbf{A}\Lambda\mathbf{A}^T\mathbf{V} - \mathbf{A}\Lambda\mathbf{E} - \mathbf{A}\Phi = 0 \quad (1)$$

where \mathbf{A} , Λ , \mathbf{V} , and \mathbf{E} are the matrices of the incidence, branch permeance, node magnetic potential, and branch MMF, respectively. Φ is the air-gap flux matrix, where $\Phi = [\varphi_{sk}, \varphi_{tk}, \varphi_{s(k+1)}, \varphi_{t(k+1)} \dots]$. The calculation flowchart of MCM is given in Fig. 2.

In order to obtain the air-gap flux, the analytical model of slotted air-gap field is proposed using the improved CPM rather than subdomain model to consider slotting effect and reduce the computational burden. Comparing with the subdomain model, the improved CPM based on the conformal transformation can account for arbitrary groove type and tooth-tip with high accuracy. The complex permeance function is extracted from only one-slot region, which can reduce the calculation time while keeping the same high accuracy, as shown in the blue region of Fig. 3(a).

Three conformal transformations are used to calculate the complex permeance function for both slotted and slotless air-gap region [32]

$$\frac{B_S}{B_\Psi} = \left(\frac{\partial \Psi}{\partial W} \right)^* \left(\frac{\partial W}{\partial Z} \right)^* \left(\frac{\partial Z}{\partial S} \right)^* \quad (2)$$

where

$$Z = \ln S \quad (3)$$

$$Z = g(W) = A_0 \int \prod_{k=1}^{n-1} (W - w_k)^{-\frac{\alpha_k}{\pi} - 1} dw + C_0 \quad (4)$$

$$\Psi = e^{-j\pi \left(\frac{2W - jw_b}{Q_s w_a} - 1 \right)} \quad (5)$$

where A_0 , w_k , α_k , and C_0 are the Schwarz–Christoffel (SC) parameters and can be obtained from SC transformation. Q_s is the slot number.

As both slotted and slotless air-gap region will mapping to the same annulus in the Ψ domain of Fig. 3(d₁) and (d₂) using the same conformal transformations of (3)–(5), the improved complex permeance function that represents the relationship between slotted and slotless air-gap can be expressed as

$$\lambda = \left(\frac{B_{S_slotted}}{B_{\Psi_slotted}} \right) / \left(\frac{B_{S_slotless}}{B_{\Psi_slotless}} \right) = \lambda_a + j\lambda_b. \quad (6)$$

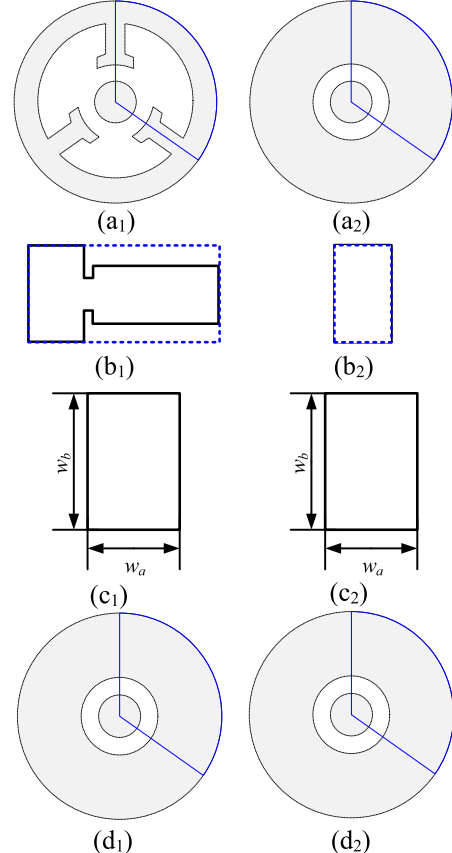


Fig. 3. Conformal transformations based on one-slot region. (a₁) Slotted S domain. (a₂) Slotless S domain. (b₁) Slotted Z domain. (b₂) Slotless Z domain. (c₁) Slotted W domain. (c₂) Slotless W domain. (d₁) Slotted Ψ domain. (d₂) Slotless Ψ domain.

Thus, the radial and tangential component of slotted air-gap field can be obtained by

$$B_r = \lambda_a \left[B_{mr} + \sum_k B_{cr}(i_{sk}) \right] + \lambda_b \left[B_{m\alpha} + \sum_k B_{c\alpha}(i_{sk}) \right] \quad (7)$$

$$B_\alpha = \lambda_a \left[B_{m\alpha} + \sum_k B_{c\alpha}(i_{sk}) \right] - \lambda_b \left[B_{mr} + \sum_k B_{cr}(i_{sk}) \right] \quad (8)$$

where B_{mr} , $B_{m\alpha}$, B_{cr} , and $B_{c\alpha}$ are the radial and tangential component of slotless air-gap field produced by the PMs and the equivalent current including winding current and iron nonlinearity, respectively [28]. The equivalent current i_{sk} is calculated using

$$i_{sk} = -(V_{(k+1)} - V_k) \quad (9)$$

where V_k and $V_{(k+1)}$ are the adjacent magnetic potentials.

Then, the air-gap flux source in Fig. 1, which is similar to the voltage controlled current source, is calculated by the integral

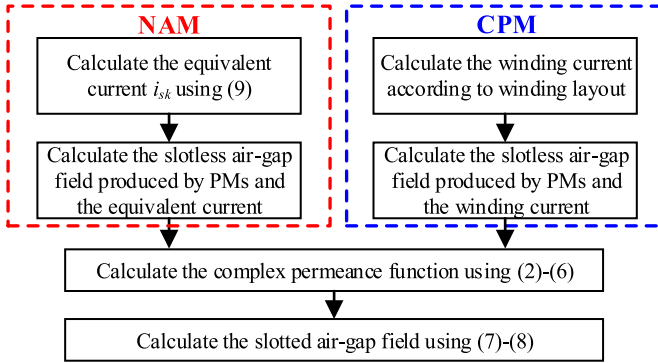


Fig. 4. Flowchart of calculating the air-gap field.

of the air-gap flux density

$$\varphi_{ik} = l_{ef} r \int_{\alpha_{i1}}^{\alpha_{i2}} B_r(r, \alpha) d\alpha, \text{ where } i = t, s \quad (10)$$

where l_{ef} is the active length of the motor. The calculation flowchart of the analytical model is given in Fig. 4. Finally, by solving (1) with the given rotor position and winding current, the magnetic field of SPM motor is obtained, which is essential to solve the electric circuit model and the mechanical model.

B. Electric Circuit Model

The electric circuit model is divided into two parts to obtain the transient performance of SPM motor, the control strategy and electric circuit. The control strategy, such as field-oriented control or direct torque control, gives the signal to the power semiconductor device in the VSI and therefore the winding current is produced in the electric circuit to drive the motor. In one switching cycle of power device, the output voltage is a PWM waveform generated by control strategy and it is expressed in the Fourier form

$$u_s(t) = m_p u_{s0} + \sum_{k=1}^{\infty} \frac{2u_{s0}}{\pi k} \sin(m_p k \pi) \cos(2\pi f_s k t + \alpha_{sk}) \quad (11)$$

where m_p , f_s , and u_{s0} are the duty cycle, frequency, and voltage value of PWM. α_{sk} represents the phase shift of the switching-ON status.

In the electric circuit, the nonlinear inductance matrix \mathbf{L}_{ABC} , nonlinear back EMF matrix \mathbf{E}_{ABC} , and resistance matrix \mathbf{R}_{ABC} are used to represent the three-phase voltage \mathbf{U}_{ABC} of SPM motor

$$\mathbf{U}_{ABC} = \mathbf{L} \frac{d\mathbf{I}_{ABC}}{dt} + \mathbf{R}_{ABC} \mathbf{I}_{ABC} + \mathbf{E}_{ABC} \quad (12)$$

where $\mathbf{U}_{ABC} = [u_A \ u_B \ u_C]^T$, $\mathbf{R}_{ABC} = [R_A \ R_B \ R_C]^T$

$$\mathbf{I}_{ABC} = [i_A \ i_B \ i_C]^T, \quad \mathbf{E}_{ABC} = [E_A \ E_B \ E_C]^T$$

$$\mathbf{L}_{ABC} = \begin{bmatrix} L_{AA} & M_{BA} & M_{CA} \\ M_{AB} & L_{BB} & M_{CB} \\ M_{AC} & M_{BC} & L_{CC} \end{bmatrix}.$$

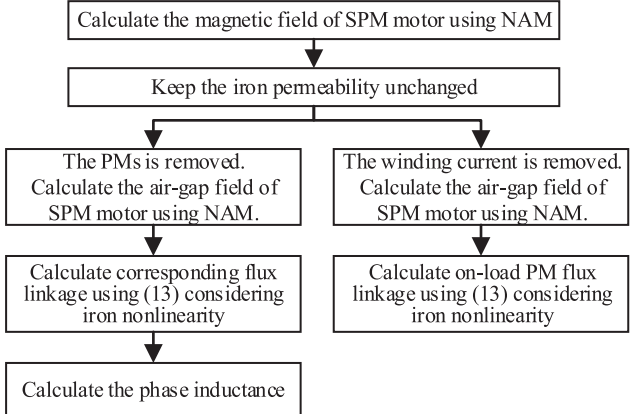


Fig. 5. Flowchart of frozen permeability method.

It is noted that the calculation of inductance is not given in [27]–[30] and the back EMF cannot be separated from the induced voltage. If the total induced voltage is used to solve the electric circuit model instead of the nonlinear inductance and back EMF, huge numerical errors will occur due to the iterative calculation of MCM in the magnetic model. Hence, this article proposes a novel method to calculate the nonlinear inductance and back EMF simultaneously based on the frozen permeability method. The phase flux linkage ψ_{ph} is calculated as

$$\psi_{ph} = N_c \sum_{i=1}^{\kappa} (\varphi_{tooth_i} + \varphi_{slot_i}) \quad (13)$$

where N_c is the number of turns in the coil. $ph \in [A, B, C]$. φ_{tooth_i} and φ_{slot_i} are the air-gap flux flowing from tooth and slot based on NAM, as shown in Fig. 1. They are obtained from the flux distribution in the magnetic circuit according to the solution of (1). Then, based on the winding layout of SPM motor, the phase flux linkage is extracted from the slot flux and air-gap flux for phases A , B , and C , as illustrated in Fig. 1. The corresponding induced voltage is the derivative of phase flux linkages. The calculation flowchart is shown in Fig. 5.

For the inductance calculation, the iron permeability is obtained from the magnetic model from (1) first and kept unchanged at the same time. Then, the air-gap flux produced by the equivalent current including winding current and iron nonlinearity is calculated using

$$B_r = \lambda_a \sum_k B_{cr}(i_{sk}) + \lambda_b \sum_k B_{ca}(i_{sk}). \quad (14)$$

Therefore, the corresponding inductance L_{ph_m} is obtained by

$$L_{ph_m} = \frac{\psi_{ph_m}}{i_{ph_w}} \quad (15)$$

where i_{ph_w} is the winding current and ψ_{ph_m} is the corresponding phase flux linkage. When the winding current is set as 1 A to the magnetic model with unchanged iron permeability, L_{ph_m} can be obtained. Similarly, the mutual inductance can be calculated using (15).

The tooth-tip leakage inductance L_{ttl} is calculated using the leakage flux flowing in the air gap outside the slot-opening. When neglecting nonlinearity, it is expressed as [34]

$$L_{ttl} = \frac{12\mu_0}{Q_s} l_{ef} N_c^2 \frac{1+g'}{2} \frac{5\delta}{5b_0 + 4\delta} \quad (16)$$

where δ is the air-gap length and b_0 is the width of slot-opening. g' represents the average value of phase shift γ_k between different phase current in the k th slot, which is expressed as [34]

$$g' = \frac{1}{2q} \sum_{k=1}^{2q} \cos \gamma_k \quad (17)$$

where q is the number of slots per pole per phase. $\gamma_k = 60^\circ$ if the coils in the k th slot belong to different phases or $\gamma_k = 0^\circ$ if the coils in the k th slot belong to the same phase.

The nonlinearity factor for tooth-tip leakage flux c_L is defined as

$$c_L = \frac{L_{ph_m}}{L_{ph_inf}} \quad (18)$$

where both L_{ph_inf} and L_{ph_m} are calculated using (15) and their air-gap field is obtained using NAM and CPM neglecting PMs, respectively. Then, the phase flux linkage produced by the winding current can be predicted according to the winding layout and the corresponding inductance can be obtained, as shown in Fig. 5.

For the end winding leakage inductance L_{ew} , it is difficult to give an accurate analytical expression due to the complex geometry of end windings and the mutual influence of three-phase current. Hence, the empirical permeance factors are employed to determine the end winding leakage inductance, which is described in [34]. Thus, the total winding inductance can be obtained by

$$L_{ph} = L_{ph} + c_L L_{ttl} + L_{ew}. \quad (19)$$

For the calculation of back EMF considering nonlinearity effect, a nonlinear back EMF coefficient c_{emf} is introduced to eliminate the numerical errors from the derivative of flux linkage to time

$$c_{emf} = \frac{\psi_{ph_emf}}{\psi_{ph_inf}} \quad (20)$$

where ψ_{ph_emf} and ψ_{ph_inf} are the on-load PM flux linkage for SPM motor from the NAM and CPM, respectively. Both of them are calculated when neglecting the winding current. Then, the phase flux linkage produced by the PMs only can be predicted according to the winding layout for ψ_{ph_inf} . As for ψ_{ph_emf} , the air-gap field produced by the PMs and the equivalent nonlinearity current is calculated according to Fig. 1, when the iron permeability stays finite and unchanged to account for iron nonlinearity using the frozen permeability method. The calculation flowchart is shown in Fig. 5. It is noted that the proposed coefficients c_L and c_{emf} are also promising for other types of motors such as interior permanent magnet (IPM) motors and vernier PM motors, which will be investigated in the future.

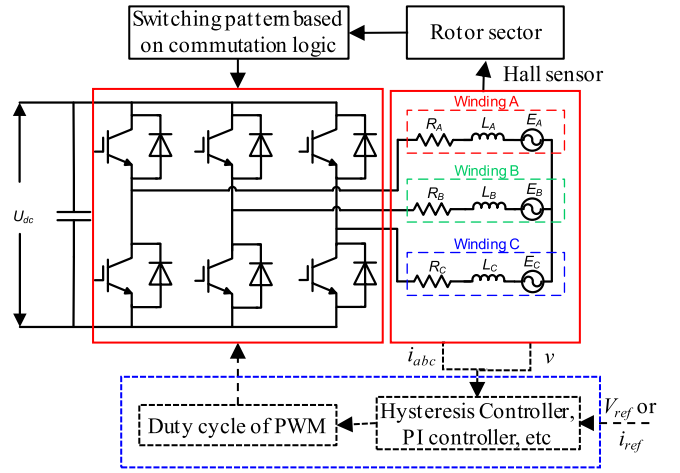


Fig. 6. Electric circuit and control strategy of the BLDC motor system.

The criterion of back EMF is obtained from the derivative of the open-circuit flux linkage to time

$$E_{ph_inf}(t) = \frac{d\psi_{ph_inf}}{dt} = \sum_{k=1}^{\infty} kp w_r \psi_{pk} \cos(kp w_r t + \theta_{ek}) \quad (21)$$

where w_r is the rotational angular speed, p is the pole pair, and ψ_{pk} and θ_{ek} are the k th harmonic amplitude and phase of flux linkage in one phase. Hence, the back EMF under on-load condition considering nonlinearity effect is calculated by

$$E_{ph}(t) = c_{emf} E_{ph_inf} = \sum_{k=1}^{\infty} kp w_r c_{emf} \psi_{pk} \cos(kp w_r t + \theta_{ek}). \quad (22)$$

For the electric circuit of conventional inverter in Fig. 6(a), the general circuit equation for three phases of SPM motor can be obtained according to Kirchhoff's law

$$\begin{cases} s_A u_A(t) + s_B u_B(t) + s_C u_C(t) = u_s(t) \\ i_A(t) + i_B(t) + i_C(t) = 0 \end{cases} \quad (23)$$

where s_A , s_B , and s_C represent the switching status of three-phase fully controlled bridge. $s_A, s_B, s_C \in [-1, 0, 1]$. The analytical solution of phase current can be obtained as

$$i_{ph}(t) = i_{ph0} + i_{phte} e^{-\frac{t}{\tau_{ph}}} + \sum_{k=1}^{\infty} i_{phkc} \cos(pw_r kt) + i_{phks} \sin(pw_r kt) \quad (24)$$

where $ph \in [A, B, C]$.

For BLDC SPM motor, the trapezoidal control technique is used to produce constant torque, as shown in Fig. 6. In fact, the control strategy including hysteresis control or proportional integral (PI) control has already been widely used in the industrial application for BLDC motor system, which can be directly utilized with NAM. To focus on the effectiveness of the proposed model, the control strategy is simplified, in which the duty cycle of PWM is set as constant.

In the electric circuit, there are two general states: one is two-phase-current mode at steady-state condition and the other is three-phase-current mode at commutation condition. When the current is only in phases *A* and *C* at steady-state condition, the corresponding value of phase *A* in (24) can be obtained as

$$\begin{aligned} i_{At} &= i_{tA0} - \frac{u_{s0}}{z_1} - \sum_{k=1}^{\infty} i_{Ak} \\ i_{Ak} &= -\frac{\sqrt{3}kpw_r c_{emf} \psi_{Ak}}{z_1^2 + z_2^2} \left[z_1 \cos \left(\theta_{Aek} + \frac{\pi}{6} \right) \right. \\ &\quad \left. - z_2 \sin \left(\theta_{Aek} + \frac{\pi}{6} \right) \right] \end{aligned} \quad (25)$$

where i_{tA0} is the initial current of phase *A*

$$\begin{aligned} z_1 &= R_A + R_C \\ z_2 &= (L_A + M_{CA} + L_C + M_{AC}) kpw_r \\ \tau_A &= \frac{L_A + M_{CA} + L_C + M_{AC}}{R_A + R_C}. \end{aligned}$$

When there is commutation from phase *B* to phase *C* at commutation condition, the corresponding winding current in (24) can be obtained as

$$\begin{aligned} i_{At} &= i_{tA0} + \frac{R_B}{z_1} u_{s0} - \sum_{k=1}^{\infty} i_{Ak} \\ i_{Bt} &= i_{tB0} - \frac{R_A}{z_1} u_{s0} - \sum_{k=1}^{\infty} i_{Bk} \\ i_{Ct} &= -i_{At} - i_{Bt} \\ \mathbf{I}_k &= \mathbf{Z}_k^{-1} * \mathbf{U}_k \end{aligned} \quad (26)$$

where i_{tB0} is the initial current of phase *B*

$$\begin{aligned} \tau_A &= \frac{L_A}{R_A} \\ \tau_B &= \frac{L_B}{R_B} \\ z_3 &= R_A R_C + R_A R_B + R_C R_B \\ \mathbf{I}_k &= [i_{Ak} \ i_{Aks} \ i_{Bkc} \ i_{Bks}]^T \\ \mathbf{Z}_k &= \begin{bmatrix} L_B kpw_r & R_B & L_C kpw_r & -R_C \\ R_B & L_B kpw_r & -R_C & -L_C kpw_r \\ R_A & L_A kpw_r & R_A + R_C & (L_A + L_C) kpw_r \\ L_A p_w_r k & -R_A & (L_A + L_C) kpw_r & -(R_A + R_C) \end{bmatrix} \\ \mathbf{U}_k &= \sqrt{3} kpw_r c_{emf} \psi_A \\ &\quad \times [\cos(\theta_{ek}) \sin(\theta_{ek}) \cos(\theta_{ek} + \frac{\pi}{6}) \sin(\theta_{ek} + \frac{\pi}{6})]^T. \end{aligned}$$

It is noted that the similar expression of other phase current under either steady-state condition or commutation condition can be accordingly obtained using (23)–(24). It is important to choose the proper time interval for obtaining the accurate winding current in the calculation, as the rotor speed is regarded as constant during the time interval.

C. Mechanical Model

According to the Maxwell tensor theory, the torque calculation of the SPM motor is expressed as

$$T_e = \frac{1}{\mu_0} l_{efr} r^2 \int_0^{2\pi} B_r B_\alpha d\alpha. \quad (27)$$

Based on the rotational equation, the mechanical model is expressed as

$$T_e - T_{load} = J_0 \beta + B w_r \quad (28)$$

where β represents the angular acceleration, T_{load} represents the load torque, and B is the coefficient of viscosity. Hence, the rotor speed and position can be numerically obtained. Accordingly, the drive signal of VSI in the external electric circuit is determined to solve the phase current.

In order to simplify the mutual influence between the torque and current in the external circuit, the torque coefficient c_t , which represents nonlinearity effect on the torque value, is introduced to replace the complicated torque equation (27)

$$c_t = \frac{T_{e_non}}{T_{e_inf}} \quad (29)$$

where T_{e_non} is obtained using NAM considering nonlinearity effect and T_{e_inf} is predicted using CPM neglecting iron nonlinearity. It is note that the torque coefficient c_t will be redetermined at the beginning of every time interval and stays unchanged during the corresponding time interval to calculate the next rotor position for both magnetic model and electric circuit model.

D. Solving Process

As shown in Fig. 7, the solving process of NAM combines magnetic model, electric circuit model, and mechanical model in series to obtain the winding current. There are two iterative loops in the solving process. The outer loop obtains three phase current in electric circuit model and determined the rotor position in the mechanical model, whereas the inner loop gives the air-gap flux flowing to the stator of the SPM motor considering nonlinearity effect. As for CPM, the linear analytical model is used to directly obtain the phase inductance and therefore only one solving loop is used for predicting the circuit current and torque. Compared with the FEM cosimulation, the NAM significantly decreases its calculation in the magnetic model due to the reduced node in the MCM and the simplified air-gap field model using CPM. Besides, as the iron nonlinearity is represented by equivalent nonlinearity current, the NAM will achieve higher accuracy of motor performance than CPM.

III. FE CALCULATION AND EXPERIMENT VALIDATION

A 15-slot/4-pole SPM motor was built to verify the proposed models under VSI, as shown in Fig. 8. The motor was driven by VSI using trapezoidal control technique in Fig. 9. Its main parameters are given in Table I. In the three-phase full-bridge inverter of Fig. 3, dc voltage supply is 20 V. The typical forward voltage of the insulated gate bipolar transistor (IGBT) is 1.5 V from the datasheet.

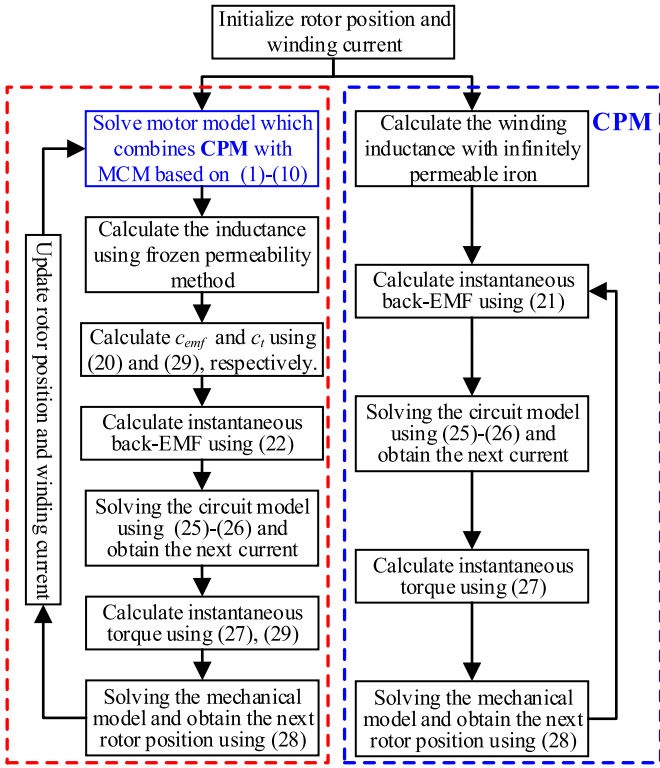


Fig. 7. Flowchart of calculating the NAM and CPM.

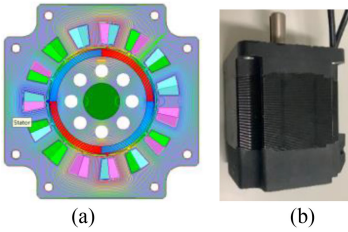


Fig. 8. 15-slot/4-pole SPM motor. (a) FE model. (b) Prototype machine.



Fig. 9. Experimental setup of SPM motor.

To analytically calculate the transient characteristic of SPM motor, the open-circuit back EMF is required to obtain the on-load nonlinear back EMF while reducing the errors of numerical calculation. Fig. 10 gives the waveforms of back EMF using CPM, NAM, FEM, and from experiment. It can be seen that both CPM and linear FEM calculation predict slightly higher fundamental harmonic back EMF than NAM and nonlinear FEM results, which shows that NAM has higher accuracy than CPM.

TABLE I
MAIN PARAMETERS OF PROTOTYPE SPM MOTOR

Parameter	Value
Stator outer length	86 mm
Stator outer radius	48 mm
Slot-opening	1.5 mm
Tooth body width	5 mm
Magnet thickness	3 mm
Pole-arc to pole-pitch ratio	1
Rotor outer radius	20 mm
Shaft radius	8 mm
Active length	55 mm
Number of parallel branches	11

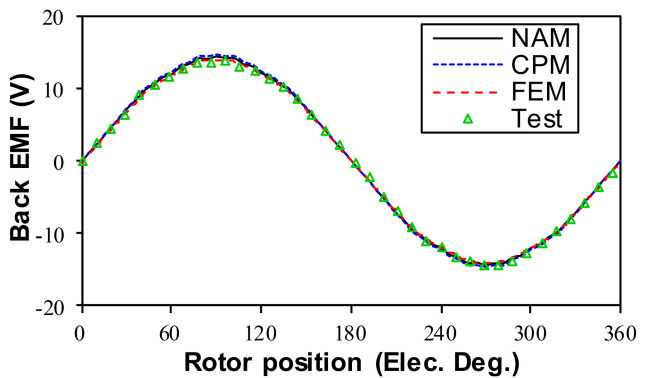


Fig. 10. Comparison of back EMF waveforms using NAM, CPM, and FEM and from experiment at 1000 r/min.

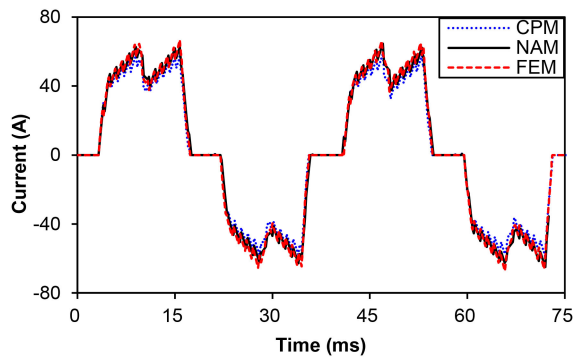


Fig. 11. Current waveform of SPM motor at 800 r/min.

When the SPM motor is operated at the constant speed of 800 r/min with duty cycle of 0.8 and switching frequency (f_s) of 1 kHz in the external circuit using trapezoidal control technique, its transient characteristic can be obtained using CPM, NAM, and FEM to investigate the influence of VSI on the motor performance. Fig. 11 illustrates that the NAM prediction of current waveform agrees well with FEM calculation but CPM underestimates the current value at constant speed. The larger errors of CPM prediction come from the overestimated back EMF amplitude and inductance using CPM due to neglecting the nonlinearity effect of SPM motor compared with NAM and FEM at the same rotational speed. Therefore, the induced voltage of SPM motor predicted using CPM is larger than that using

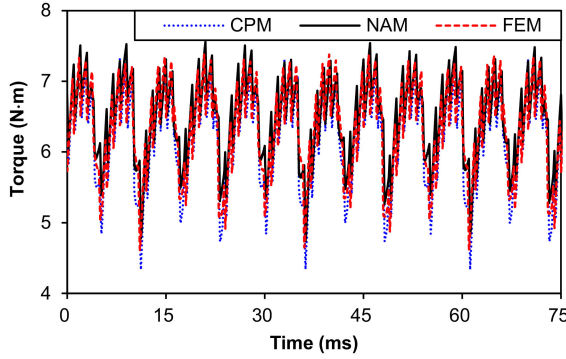


Fig. 12. Torque waveform of SPM motor at 800 r/min.

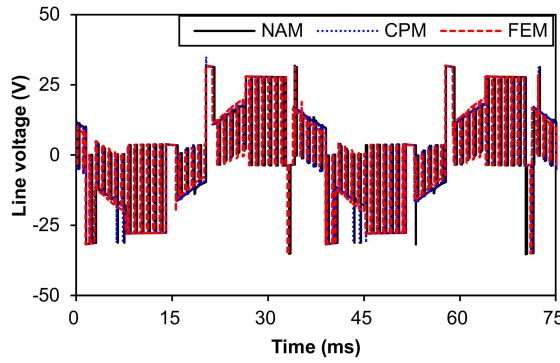


Fig. 13. Line voltage of SPM motor at 800 r/min.

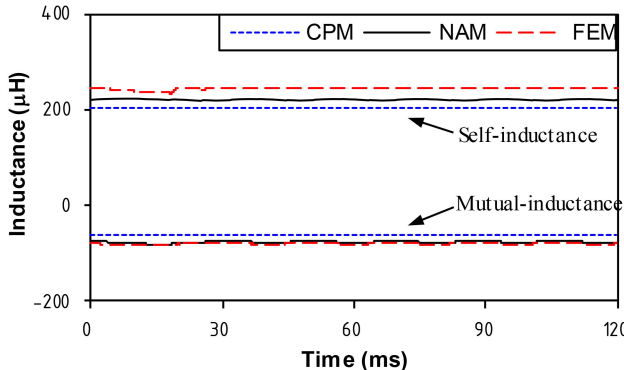


Fig. 14. Phase inductance of SPM motor at start-up with duty cycle of 0.8 and constant torque of 1 N·m.

NAM or FEM. With the same phase resistance and VSI, CPM will underestimate the current value. Similar observation can be found in the torque waveform of Fig. 12. As for the line voltage waveform of Fig. 13, both CPM and NAM have high accuracy, which means that the iron nonlinearity has a small influence on the on-load back EMF.

Then, the SPM motor is operated at constant torque from stationary condition. The external circuit is driven according to the rotor position from the Hall sensor with duty cycle of 0.8 and switching frequency (f_s) of 10 kHz. From the comparison of phase inductance in Fig. 14, NAM prediction is closer to FEM results than CPM in both self-inductance and mutual-inductance,

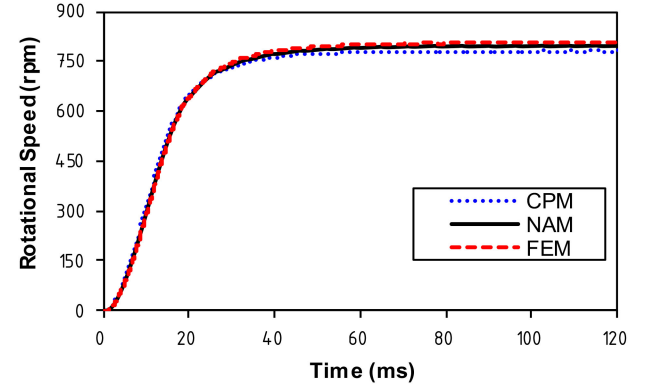


Fig. 15. Start-up speed of SPM motor with duty cycle of 0.8 and constant torque of 1 N·m.

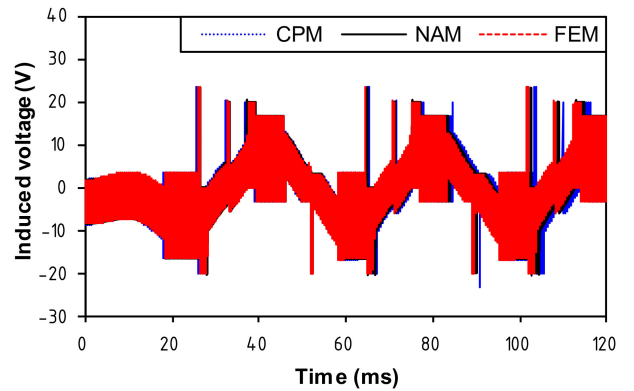


Fig. 16. Line voltage waveform of SPM motor at start-up with duty cycle of 0.8 and constant torque of 1 N·m.

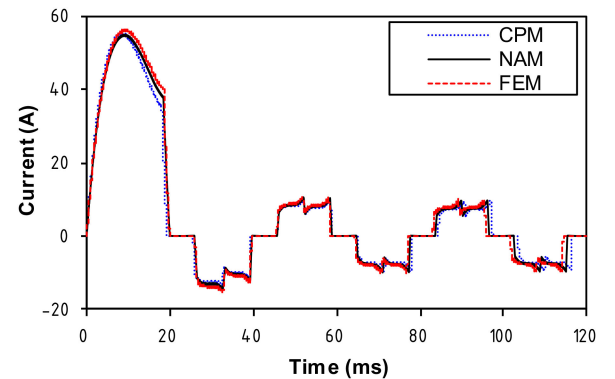


Fig. 17. Current waveform of SPM motor at start-up with duty cycle of 0.8 and constant torque of 1 N·m.

which improves the accuracy of the proposed model for transient analysis. The start-up speed of Fig. 15 shows that the NAM can accurately follow the speed of FEM calculation, whereas CPM has a static error at constant torque of 1 N·m due to the large errors of back EMF and inductance. In Fig. 16, both CPM and NAM can accurately predict the initial voltage amplitude, but CPM shows low accuracy in predicting the phase and frequency of voltage. In Figs. 17 and 18, the predicted current and torque

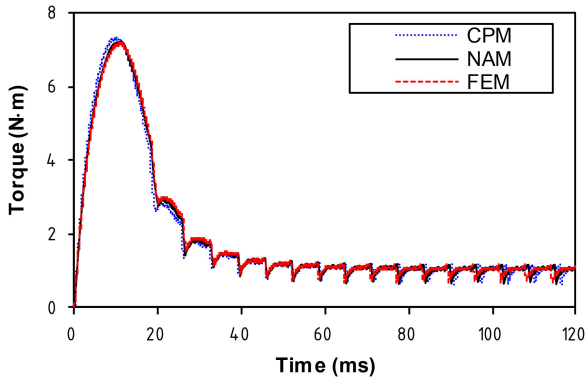


Fig. 18. Torque waveform of SPM motor at start-up with duty cycle of 0.8 and constant torque of 1 N·m.

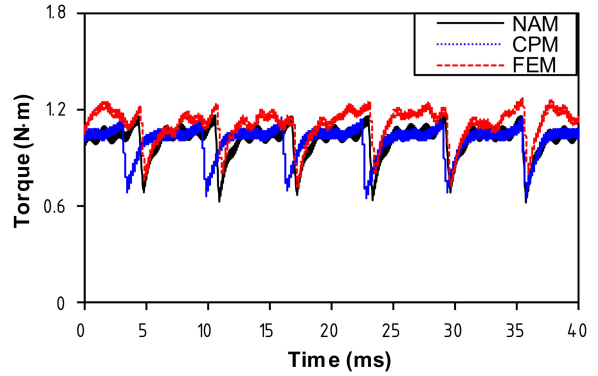


Fig. 21. Steady state of torque waveform in the SPM motor with duty cycle of 0.8 and constant torque of 1 N·m.

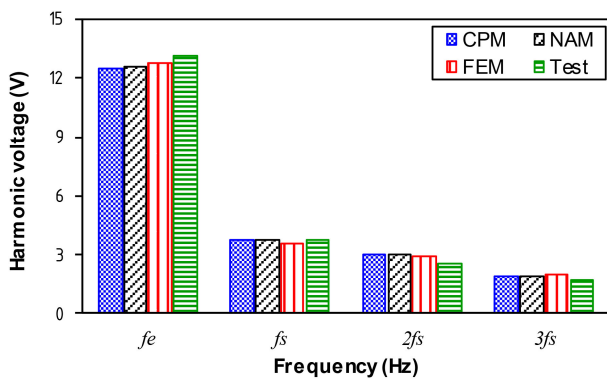


Fig. 19. Steady state of induced voltage waveform in the SPM motor with duty cycle of 0.8 and constant torque of 1 N·m.

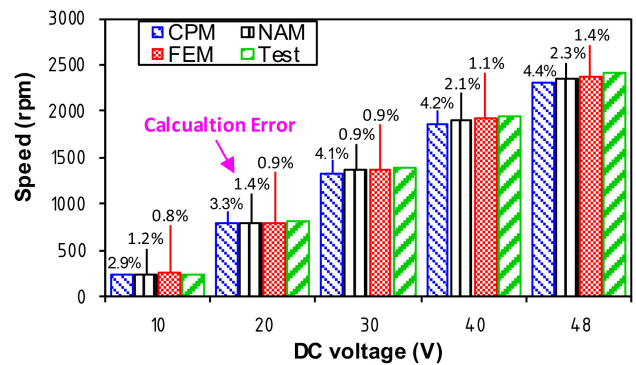


Fig. 22. Variation of steady speed to dc voltage for SPM motor with duty cycle of 0.8 and constant torque of 1 N·m.

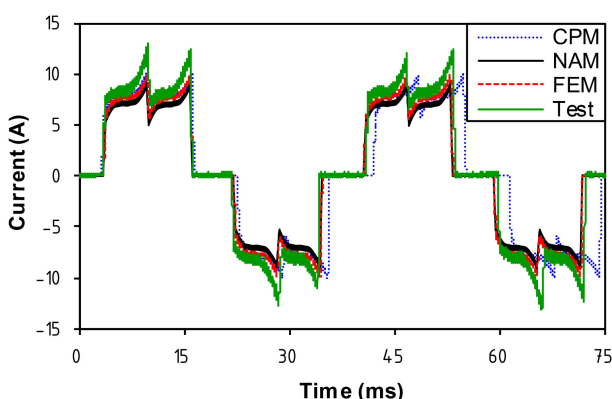


Fig. 20. Steady state of current waveform in the SPM motor with duty cycle of 0.8 and constant torque of 1 N·m.

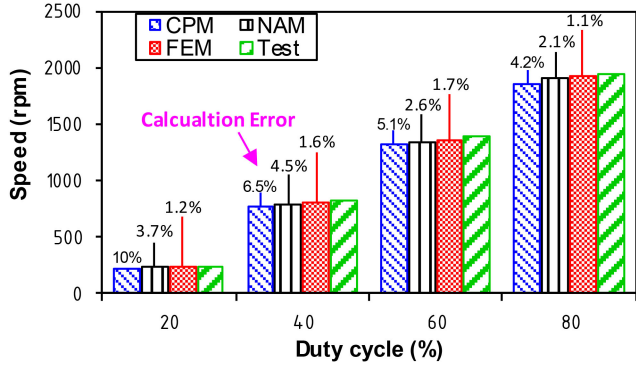


Fig. 23. Variation of steady speed to dc voltage for SPM motor with dc voltage of 40 V and constant torque of 1 N·m.

using NAM agree well with FEM results. As for CPM, large errors are observed in the phase and frequency for both current and torque at start-up.

When the SPM motor reached steady state at duty cycle of 0.8 and constant torque of 1 N·m, the harmonic line voltage and current waveform are predicted using CPM, NAM, and FEM. Their accuracy is validated by experimental results, as shown in Figs. 19 and 20. It can be seen that NAM and FEM can

predict more accurate voltage and current than CPM predictions. In Fig. 21, CPM has similar torque value to FEM result but underestimates the torque frequency, whereas NAM agrees well with FEM result. Figs. 22 and 23 show the variation of steady speed of SPM motor to the dc voltage and duty cycle at constant torque of 1 N·m and switching frequency of 10 kHz. Comparing with experimental results, both NAM and FEM show great accuracy for predicting the steady speed using VSI. The motor speed has a negligible influence on the prediction accuracy of the proposed model.

TABLE II
SIMULATION PARAMETERS FOR SPM MOTOR

Model	Air-gap tangential segment*	Total Node	Simulation time
CPM		0	
NAM	360	255	120 ms
FEM		12 134	

*The division of the circular air-gap path to show flux density distribution.

TABLE III
SOLVING TIME OF CPM, NAM, AND FEM FOR SPM MOTOR

Mode Model	Constant speed ($f_s = 1$ kHz)	Constant torque ($f_s = 10$ kHz)
CPM	254 s	1643 s
NAM	449 s	2334 s
FEM	10 588 s	478 583 s

As for the calculation resource, the main simulation parameters are listed in Table II to make a fair comparison. The FEM is running in the Ansys Maxwell platform, whereas CPM and NAM are executed in MATLAB. The total mesh node using FEM is significantly larger than the magnetic circuit node of NAM, which reflects the computational complexity in solving the magnetic model. The calculation time of CPM, NAM, and FEM is given in Table III. It can be seen that FEM consumes the largest calculation resource to predict transient characteristic of SPM motor at either constant speed or constant torque condition, whereas CPM takes the least computational time under the same work condition. Since the calculation of magnetic reluctance or finite element consumes most of the solving time, the node number is the key factor to affect calculation time. The NAM can save nearly 1/20 computational time of FEM while keeping high accuracy. Besides, the increase of carrier frequency will directly raise the computational burden, as presented in Table III. To guarantee the same calculation accuracy, it is required to give the shorter time interval and increase the calculation step in the analytical models, therefore leading to consuming longer calculation time. Thus, the proposed NAM will show a significant advantage over FEM in calculation efficiency since high switching frequency is always preferred in the advanced motor system.

IV. CONCLUSION

This article proposed the CPM and NAM to account for slotting effect for the transient analysis of SPM motor using VSI and therefore investigated the effectiveness of analytical models coupled with external circuit. In NAM, the nonlinear phase inductance and back EMF can be obtained analytically to replace the SPM motor in the drive circuit. To solve the NAM, two iterative loops are required to combine the magnetic model with electric circuit model and mechanical model. Hence, the transient performance of the SPM motor can be obtained using VSI. Compared with CPM, NAM has high accuracy to predict the electromagnetic performance of SPM motor at constant

speed or constant torque in the motor system. Besides, it saves more than 95% of the computational time using FEM.

REFERENCES

- Z. Li *et al.*, “Dynamic modeling of surface-mounted permanent magnet motors considering saturation,” in *Proc. IEEE Energy Convers. Congr. Expo.*, Sep. 2019, pp. 5624–5628.
- B.-I. Kwon, K.-I. Woo, and S. Kim, “Finite element analysis of direct thrust-controlled linear induction motor,” *IEEE Trans. Magn.*, vol. 35, no. 3, pp. 1306–1309, May 1999.
- F. Parasiliti, M. Villani, and A. Tassi, “Dynamic analysis of synchronous reluctance motor drives based on Simulink and finite element model,” in *Proc. 32nd Annu. Conf. IEEE Ind. Electron.*, 2006, pp. 1516–1520.
- M. Fasil, N. Mijatovic, B. B. Jensen, and J. Holboll, “Nonlinear dynamic model of PMLBDC motor considering core losses,” *IEEE Trans. Ind. Electron.*, vol. 64, no. 12, pp. 9282–9290, Dec. 2017.
- O. A. Mohammed, S. Liu, and Z. Liu, “A phase variable model of brushless DC motors based on finite element analysis and its coupling with external circuits,” *IEEE Trans. Magn.*, vol. 41, no. 5, pp. 1576–1579, May 2005.
- W. Zhao, M. Cheng, X. Zhu, W. Hua, and X. Kong, “Analysis of fault-tolerant performance of a doubly salient permanent-magnet motor drive using transient cosimulation method,” *IEEE Trans. Ind. Electron.*, vol. 55, no. 4, pp. 1739–1748, Apr. 2008.
- L. Di Leonardo, F. Parasiliti, M. Tursini, and M. Villani, “Transient analysis of PM synchronous motor drives by finite element model co-simulation,” in *Proc. 39th Annu. Conf. IEEE Ind. Electron. Soc.*, 2013, pp. 6834–6840.
- M. A. Jabbar, Z. Liu, and J. Dong, “Time-stepping finite-element analysis for the dynamic performance of a permanent magnet synchronous motor,” *IEEE Trans. Magn.*, vol. 39, no. 5, pp. 2621–2623, Sep. 2003.
- L. Quéval and H. Ohsaki, “Nonlinear abc-model for electrical machines using N-D lookup tables,” *IEEE Trans. Energy Convers.*, vol. 30, no. 1, pp. 316–322, Mar. 2015.
- J. Wu, J. Wang, C. Gan, Q. Sun, and W. Kong, “Efficiency optimization of PMSM drives using field-circuit coupled FEM for EV/HEV applications,” *IEEE Access*, vol. 6, pp. 15192–15201, 2018.
- T. N. Matzen and P. O. Rasmussen, “Modelling magnetic saturation effects in IPMSMs for use in sensorless saliency based methods,” in *Proc. Eur. Conf. Power Electron. Appl.*, 2007, pp. 1–8.
- Y. Kano, K. Watanabe, T. Kosaka, and N. Matsui, “A novel approach for circuit-field-coupled time-stepping electromagnetic analysis of saturated interior PM motors,” *IEEE Trans. Ind. Appl.*, vol. 45, no. 4, pp. 1325–1333, Jul./Aug. 2009.
- M. Fazil and K. R. Rajagopal, “Nonlinear dynamic modeling of a single-phase permanent-magnet brushless DC motor using 2-D static finite-element results,” *IEEE Trans. Magn.*, vol. 47, no. 4, pp. 781–786, Apr. 2011.
- G. Luo, R. Zhang, Z. Chen, W. Tu, S. Zhang, and R. Kennel, “A novel nonlinear modeling method for permanent-magnet synchronous motors,” *IEEE Trans. Ind. Electron.*, vol. 63, no. 10, pp. 6490–6498, Oct. 2016.
- W. Liang, J. Wang, T. Lu, and W. Fang, “A new method for multiple finite-element models in cosimulation with electrical circuit using machine multiloop modeling scheme,” *IEEE Trans. Ind. Electron.*, vol. 61, no. 12, pp. 6583–6590, Dec. 2014.
- M. Tursini, M. Villani, A. Di Tullio, G. Fabri, and F. P. Collazzo, “Nonlinear model suitable for the offline cosimulation of fault-tolerant PM motors drives,” *IEEE Trans. Ind. Appl.*, vol. 53, no. 4, pp. 3719–3729, Jul. 2017.
- X. Huang, M. Zhu, W. Chen, J. Zhang, and Y. Fang, “Dynamic reluctance mesh modeling and losses evaluation of permanent magnet traction motor,” *IEEE Trans. Magn.*, vol. 53, no. 6, Jun. 2017, Art. no. 8102804.
- F. Chai, L. Gan, and Y. Yu, “Magnetic field analysis of an iron-cored tiered type permanent magnet spherical motor using modified dynamic reluctance mesh method,” *IEEE Trans. Ind. Electron.*, vol. 67, no. 8, pp. 6742–6751, Aug. 2020.
- F. E. Fleming and C. S. Edrington, “Real-time emulation of switched reluctance machines via magnetic equivalent circuits,” *IEEE Trans. Ind. Electron.*, vol. 63, no. 6, pp. 3366–3376, Jun. 2016.
- M. Fukuoka, K. Nakamura, and O. Ichinokura, “Dynamic analysis of planetary-type magnetic gear based on reluctance network analysis,” *IEEE Trans. Magn.*, vol. 47, no. 10, pp. 2414–2417, Oct. 2011.
- D. Cao, W. Zhao, J. Ji, and Y. Wang, “Parametric equivalent magnetic network modeling approach for multi-objective optimization of PM machine,” *IEEE Trans. Ind. Electron.*, vol. 68, no. 8, pp. 6619–6629, Aug. 2021.

- [22] L. Mine, S. Goyal, and A. A. E. Abdallah, "Improved dynamic modeling of squirrel-cage induction machines using magnetic reluctance network theory," in *Proc. 21st Int. Conf. Elect. Mach. Syst.*, 2018, pp. 555–559.
- [23] V. Z. Faradonbeh, A. Rahideh, M. M. Ghahfarokhi, E. Amiri, A. D. Aliabad, and G. A. Markadeh, "Analytical modeling of slotted, surface-mounted permanent magnet synchronous motors with different rotor frames and magnet shapes," *IEEE Trans. Magn.*, vol. 57, no. 1, Jan. 2021, Art. no. 8100413.
- [24] S. G. Min and B. Sarlioglu, "Analytical prediction and multiconstrained nonlinear optimization of slotted linear PM motors taking into account two-dimensional end effects," *IEEE Trans. Ind. Electron.*, vol. 67, no. 4, pp. 2965–2976, Apr. 2020.
- [25] X. Wang, Q. Li, S. Wang, and Q. Li, "Analytical calculation of air-gap magnetic field distribution and instantaneous characteristics of brushless DC motors," *IEEE Trans. Energy Convers.*, vol. 18, no. 3, pp. 424–432, Sep. 2003.
- [26] H. V. Xuan, H. Polinder, D. Lahaye, and J. A. Ferreira, "Modeling for the design of fractional slot PM machines with concentrated windings protected from demagnetization during three-phase short circuit," in *Proc. IEEE Energy Convers. Congr. Expo.*, 2012, pp. 1276–1283.
- [27] L. J. Wu, Z. Li, X. Huang, Y. Zhong, Y. Fang, and Z. Q. Zhu, "A hybrid field model for open-circuit field prediction in surface-mounted PM machines considering saturation," *IEEE Trans. Magn.*, vol. 54, no. 6, Jun. 2018, Art. no. 8103812.
- [28] L. J. Wu, Z. Li, D. Wang, H. Yin, X. Huang, and Z. Q. Zhu, "On-load field prediction of surface-mounted PM machines considering nonlinearity based on hybrid field model," *IEEE Trans. Magn.*, vol. 55, no. 3, Mar. 2019, Art. no. 8100911.
- [29] L. Wu, H. Yin, D. Wang, and Y. Fang, "A nonlinear subdomain and magnetic circuit hybrid model for open-circuit field prediction in surface-mounted PM machines," *IEEE Trans. Energy Convers.*, vol. 34, no. 3, pp. 1485–1495, Sep. 2019.
- [30] L. Wu, H. Yin, D. Wang, and Y. Fang, "On-load field prediction in SPM machines by a subdomain and magnetic circuit hybrid model," *IEEE Trans. Ind. Electron.*, vol. 67, no. 9, pp. 7190–7201, Sep. 2020.
- [31] S. Li, W. Tong, M. Hou, S. Wu, and R. Tang, "Analytical model for no-load electromagnetic performance prediction of V-shape IPM motors considering nonlinearity of magnetic bridges," *IEEE Trans. Energy Convers.*, vol. 37, no. 2, pp. 901–911, Jun. 2022.
- [32] K. Boughrara, R. Ibtiouen, D. Zarko, O. Touhami, and A. Rezzoug, "Magnetic field analysis of external rotor permanent-magnet synchronous motors using conformal mapping," *IEEE Trans. Magn.*, vol. 46, no. 9, pp. 3684–3693, Sep. 2010.
- [33] V. Ostovic, *Dynamics of Saturated Electric Machines*. New York, NY, USA: Springer-Verlag, 1989.
- [34] J. Pyrhönen, T. Jokinen, and V. Hrabovcova', *Design of Rotating Electrical Machines*. Chichester, U.K.: Wiley, 2008, pp. 225–253.